



H₂O₂ Photosynthesis Hot Paper

How to cite: Angew. Chem. Int. Ed. **2025**, e202506963 doi.org/10.1002/anie.202506963

Unlocking One-Step Two-Electron Oxygen Reduction via Metalloid Boron-Modified Zn₃In₂S₆ for Efficient H₂O₂ Photosynthesis

Ji-Li Zhou, Yan-Fei Mu,* Meng Qiao, Meng-Ran Zhang, Su-Xian Yuan, Min Zhang,* and Tong-Bu Lu*

Abstract: The indirect two-step two-electron oxygen reduction reaction ($2e^-$ ORR) dominates photocatalytic H_2O_2 synthesis but suffers from sluggish kinetics, ${}^{\bullet}O_2^-$ -induced catalyst degradation, and spatiotemporal carrier-intermediate mismatch. Herein, we pioneer a metal-metalloid dual-site strategy to unlock the direct one-step $2e^-$ ORR pathway, demonstrated through boron-engineered $Zn_3In_2S_6$ (**B-ZnInS**) photocatalyst with In-B dual-active sites. The In-B dual-site configuration creates a charge-balanced electron reservoir by charge complementation, which achieves moderate O_2 adsorption via bidentate coordination and dual-channel electron transfer, preventing excessive O—O bond activation. Simultaneously, boron doping induces lattice polarization to establish a built-in electric field, quintupling photogenerated carrier lifetimes versus pristine **ZnInS**. These synergies redirect the O_2 activation pathway from indirect to direct $2e^-$ ORR process, delivering an exceptional H_2O_2 production rate of 3121 μ mol g^{-1} h^{-1} in pure water under simulated AM 1.5G illumination (100 mW cm $^{-2}$)—an 11-fold enhancement over **ZnInS**. The system achieves an unprecedented apparent quantum yield of 49.8% at 365 nm for H_2O_2 photosynthesis among inorganic semiconducting photocatalysts, and can continuously produce medical-grade H_2O_2 (3 wt%). This work provides insights for designing efficient H_2O_2 photocatalysts and beyond.

Introduction

Hydrogen peroxide (H_2O_2) , an environmentally benign oxidant, is extensively utilized in chemical manufacturing, healthcare, and environmental remediation. However, over 95% of industrial H_2O_2 production still relies on the energy-intensive anthraquinone process, which generates substantial waste and requires hazardous organic solvents. Photocatalytic H_2O_2 synthesis via the two-electron oxygen reduction reaction $(2e^- \ ORR)$ has emerged as a sustainable alternative under global decarbonization efforts. In the direct one-step $2e^- \ ORR$ $(O_2 + 2e^- + 2H^+ \rightarrow H_2O_2)$ and ii) the indirect two-step $2e^- \ ORR$ pathway involving a superoxide radical intermediate $(O_2 + e^- = {}^{\bullet}O_2^-; {}^{\bullet}O_2^- + e^- + 2H^+ \rightarrow H_2O_2)$. While the indirect pathway

dominates conventional systems, its multi-step nature causes kinetic limitations due to spatiotemporal mismatch with transient carrier dynamics. Moreover, the strong oxidizing ${}^{\bullet}O_2^-$ intermediate can damage catalyst structures, leading to catalyst degradation and photocarrier waste. [13] In contrast, the direct one-step pathway is thermodynamically favorable and bypasses ${}^{\bullet}O_2^-$ intermediate formation, thereby accelerating the reaction kinetics and enhancing photocarrier utilization efficiency for H_2O_2 generation. [14] These fundamental differences underscore the urgent need to develop photocatalysts specifically engineered for the direct one-step $2e^-$ ORR pathway to achieve efficient H_2O_2 photosynthesis.

To date, studies on direct pathways for H₂O₂ photosynthesis remain scarce, with mechanistic studies primarily focusing on the alterations of adsorption energy and intermediate free energy.^[15,16] Crucially overlooked, the photocarrier evolution dynamics fundamentally govern reaction pathways and product selectivity. In this context, catalytic sites act as pivotal bridges that simultaneously coordinate interfacial charge transfer and adsorbed-molecular activation processes.[17,18] Based on the catalytic site configurations, O2 adsorption modes over the catalyst can be categorized into two primary types: the Pauling adsorption at single-site and the Yeager adsorption at dual-site.^[19] In Pauling adsorption (Scheme 1a), monodentate O-atom anchoring induces spatial asymmetry in orbital coupling between O₂ and the catalyst. [20-22] This anisotropic configuration constrains carrier migration along a unidirectional pathway via the adsorbed O atom, while leaving the distal O atom electronically isolated due to orbital decoupling. The resultant carrier localization restricts electron injection exclusively to the proximal π^* -orbital,

MOE International Joint Laboratory of Materials Microstructure, Institute for New Energy Materials and Low Carbon Technologies, School of Materials Science and Engineering, Tianjin University of Technology, Tianjin 300384, China

E-mail: 007916@yzu.edu.cn

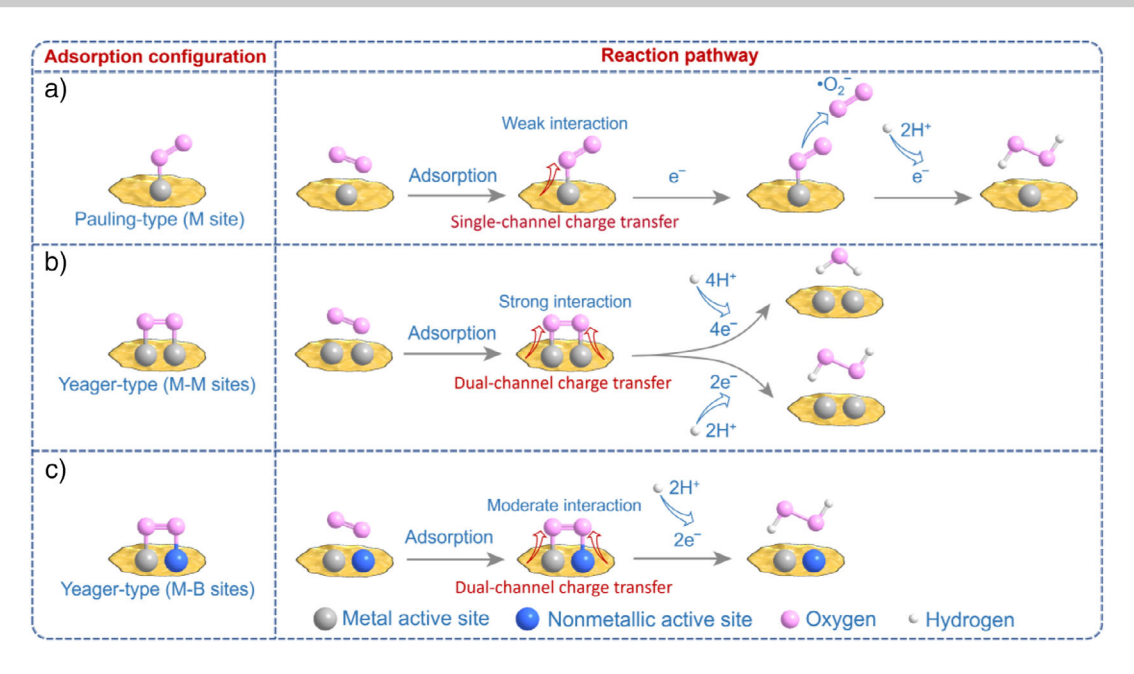
zm2016@email.tjut.edu.cn lutongbu@tjut.edu.cn

Dr. Y.-F. Mu

School of Chemistry and Chemical Engineering, Yangzhou University, Yangzhou, Jiangsu 225002, China

Additional supporting information can be found online in the Supporting Information section

^[*] J.-L. Zhou, Dr. Y.-F. Mu, M. Qiao, M.-R. Zhang, S.-X. Yuan, Dr. M. Zhang, Prof. Dr. T.-B. Lu



Scheme 1. Schematic of ORR pathways based on a) Pauling adsorption at single-site, b) Yeager adsorption at dual metal sites, and c) Yeager adsorption at metal-boron dual-sites.

dynamically prohibiting the simultaneous population of both orbitals. Such compartmentalized carrier dynamics inherently precludes direct synchronized 2e⁻ transfer, necessitating a metastable intermediate-mediated two-step electron transfer mechanism. Conversely, Yeager adsorption (Scheme 1b) enables symmetric π^* -orbital coupling through bidentate O₂ coordination on dual-metal sites, theoretically allowing concerted 2e⁻ transfer.^[23] Nevertheless, excessive metal-O₂ electronic interaction in conventional dual-site catalysts often over-weaken the O-O bond (even cleavage), favoring 4e-ORR to H₂O rather than selective H₂O₂ formation. [24-26] This dichotomy highlights the critical need for dual-site catalysts with moderate O₂ coupling strength to balance activation energy and charge transfer efficiency, ultimately steering selective 2e⁻ ORR without bond cleavage. Metalloid boron, characterized by its electron-deficient nature and metalnonmetal hybrid properties,^[27] serves as an ideal candidate for constructing dual-active sites. When paired with metals (forming M-B systems), the electron deficiency of boron is mitigated through charge redistribution with adjacent metal atoms, establishing a balanced electron reservoir.^[28] This synergy fine-tunes orbital coupling strength with O_2 , strategically avoiding excessive population of π^* antibonding orbitals that would otherwise destabilize the O-O bond. Consequently, the M-B dual sites orchestrate synchronous electron transfer via dual-channel pathways (Scheme 1c), effectively driving direct one-step 2e⁻ ORR while preserving the O-O bond integrity.

Herein, we demonstrate a boron-engineered $Zn_3In_2S_6$ (**B-ZnInS**) photocatalyst that achieves one-step $2e^-$ oxygen reduction for efficient H_2O_2 photosynthesis through modulation of In-B electronic structure and photocarrier dynamics. The constructed In-B dual-active sites enable optimal O_2 activation with charge complementation effect, avoiding O—O bond-breaking while enabling a synchronous

population of π^* -orbitals via dual-channel charge transfer. Concurrently, boron-induced lattice polarization creates an internal electric field in **B-ZnInS** that spatially separates photogenerated carriers, prolonging their lifetime fivefold compared to pristine **ZnInS**. These concerted effects shift the O_2 activation mechanism from indirect stepwise $2e^-$ transfers to direct single-step $2e^-$ pathway, delivering a high H_2O_2 production rate of 3121 μ mol g^{-1} h^{-1} in pure water under simulated sunlight—an 11 times higher than **ZnInS**. Notably, the system achieves a record apparent quantum yield of 49.8% at 365 nm among inorganic semiconductor photocatalysts.

Results and Discussion

Synthesis and Characterization of B-ZnInS

A series of boron-modified zinc indium sulfide (B-ZnInS) photocatalysts were synthesized through a two-step approach (Figure 1a, experimental details in the Supporting Information). Initially, pristine Zn₃In₂S₆ (abbreviated as **ZnInS**) was hydrothermally prepared using zinc acetate (Zn(AC)₂), indium chloride (InCl₃) and thioacetamide (TAA) precursors.^[29] Boron was then incorporated into the ZnInS matrix through NaBH₄ pyrolysis, yielding samples labeled B_x -ZnInS (x = 15, 20, 25) on nominal doping levels. Inductively coupled plasma mass spectrometry (ICP-MS) measurements revealed actual boron contents (mass fractions) of 0.66%, 1.75%, and 3.05% for \mathbf{B}_{15} -, \mathbf{B}_{20} -, and \mathbf{B}_{25} -**ZnInS**, respectively (Figure S1 and Table S1). Unless specified, B-ZnInS hereafter refers to B20-ZnInS, which was selected as the primary focus of this study. The X-ray diffraction (XRD) patterns (Figure 1b) indicate that pristine **ZnInS** can be indexed to P-3m1(164) hexagonal phase (PDF

wnloaded from https://onlinelibrary.wiley.com/doi/10.1002/anie.202506963 by Tianjin University Of, Wiley Online Library on [24/06/2025]. See the Terms

and Conditions (https://onlinelibrary.wiley.com/terms-and-conditions) on Wiley Online Library for rules of use; OA articles are governed by the applicable Creative Commons Licenson

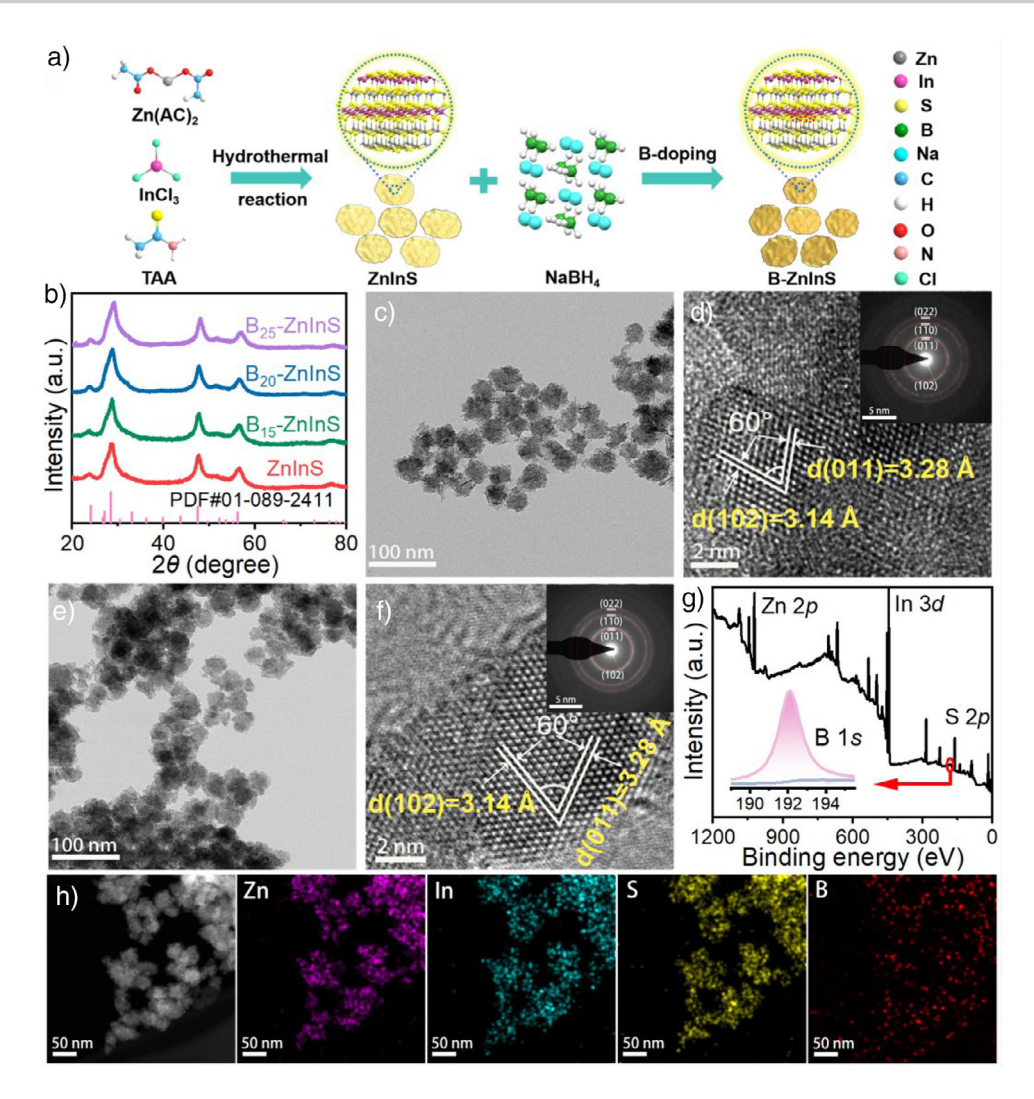


Figure 1. a) Synthetic process of B-ZnInS. b) XRD patterns of ZnInS and B-ZnInS. c) TEM and d) HRTEM images of ZnInS. e) TEM and f) HRTEM images of B-ZnInS. g) XPS spectrum and h) EDS mapping of B-ZnInS.

card no. 01–089–2411), with characteristic diffraction peaks at 24.03°, 27.15°, 28.43°, 47.17°, and 56.00°, matching the (005), (011), (102), (110), and (022) planes, respectively. Low-concentration boron doping (B_{15} -**ZnInS** and B_{20} -**ZnInS**) does not induce significant structural modifications, whereas higher boron content (B₂₅-ZnInS) triggers a shift of the diffraction peaks toward higher angles (Figure S2). This shift indicates lattice contraction, which aligns with the incorporation of smaller B³⁺ ions (compared to Zn²⁺/In³⁺) into the lattice, leading to local structural over-distortion. In addition, an additional XRD peak attributed to impurity B_2S_3 (PDF card no. 00-015-0448) appears at 20.88° for B₂₅-ZnInS, further demonstrating the disruption of the structural integrity, consistent with excessive doping-induced defects. [30,31] The transmission electron microscopy (TEM) image shows that ZnInS exhibits nanosheet morphology with an average diameter of 35-40 nm (Figures 1c and S3a). The high-resolution TEM (HRTEM) image of ZnInS (Figure 1d) exhibits two distinct lattice fringes at 3.28 Å (011) and 3.14 Å (102) with a 60° dihedral angle. These values agree well with the theoretical values for the (011) and (102)

planes in the hexagonal phase, confirming the well-defined crystalline structure (Figure S4).^[32] The selected area electron diffraction (SAED) pattern (inset of Figure 1d) of **ZnInS** displays multiple sets of diffraction rings, indicating the formation of polycrystalline structures. Boron incorporation did not alter the morphology and dimensions (Figures 1e, S3 and S5). Moreover, as depicted in Figure 1f, the HRTEM image and SAED pattern of **B-ZnInS** reveal that the lattice structure remains essentially intact upon the introduction of boron species, also presenting (011) and (102) diffraction planes with a dihedral angle of 60°, demonstrating preserved structural integrity post-doping.

High-resolution X-ray photoelectron spectroscopy (XPS) analyses (Figures 1g and S6) unequivocally confirmed the successful incorporation of boron into **B-ZnInS** nanosheets, with the B 1s XPS peak at 192.0 ± 0.2 eV diagnostic of B³+ in metal-boron-sulfide systems (versus 188.5 eV for B⁰ and 193.4 eV for B₂O₃).[³³] Energy-dispersive X-ray spectroscopy (EDS) mapping measurements (Figures 1h and S7–S10) directly visualized homogeneous spatial distribution of Zn, In, S, and B across the nanosheet. In addition, we

15213773, 0, Downloaded from https://onlinelibrary.wiley.com/doi/10.1002/anie.202506963 by Tianjin University Of, Wiley Online Library on [24.062025]. See the Terms and Conditions (https://onlinelibrary.wiley.com/terms-and-conditions) on Wiley Online Library for rules of use; OA articles are governed by the applicable Creative Commons. Licenson

Research Article

excluded the possible interference of Na species through EDS and XPS spectra (Figures S9, S11, and Tables S2, S3). To determine the doping position of boron in the B-ZnInS lattice structure, Raman spectroscopy measurements were further conducted (Figure S12). Pristine ZnInS exhibits two distinct vibrational modes near 250 cm⁻¹ (attributed to In-S (F_{2g}) signal) and 350 cm⁻¹ (corresponding to Zn-S (A_{1g}) signal), as calibrated against a silicon reference (520 cm⁻¹).[34] Boron doping induced blue-shifts (+10 cm⁻¹ for In-S and +6 cm⁻¹ for Zn-S), consistent with bond shortening according to the harmonic oscillator model.[35] Significantly, the In-S (F_{2g}) vibrational mode exhibits distortion accompanied by the emergence of a new Raman signal attributed to the B-S-In coordination network, indicating the preferential substitution of boron near In-S regions. Figure \$13 shows the electron paramagnetic resonance (EPR) spectra, and the signal at g = 2.003 corresponds to the unpaired electrons captured in sulfur vacancies.[36] Compared with pristine ZnInS, B-ZnInS exhibits higher EPR intensity, indicating that the boron occupying the sulfur vacancy increases the content of unpaired electrons via electron redistribution from adjacent indium to boron.[37]

Electronic Structure Analysis

The photocatalytic feasibilities of ZnInS and B_x-ZnInS for H₂O₂ production were evaluated through band structure analysis using UV-vis diffuse reflectance spectroscopy (UVvis DRS) and ultraviolet photoelectron spectroscopy (UPS). Despite varying boron doping levels (0.66–3.05 wt%), all samples maintained comparable light absorption profiles (Figure \$14a), indicating minimal bandgap perturbation. This stability stems from interstitial doping of boron at low concentrations, which preserves the electronic structure of the host lattice.^[38] The optical bandgap values (E_{σ}) of **ZnInS**, \mathbf{B}_{15} -, \mathbf{B}_{20} -, and \mathbf{B}_{25} -**ZnInS** were determined to be 3.14, 3.07, 3.11, and 3.11 eV, respectively, based on the Kubelka-Munk formula (Figure \$14b). Complementary UPS analysis (Figure \$15) revealed systematic band engineering induced by boron doping. The potential of valence band maximum (E_{VB}) progressively shifts downward from 2.43 V (pristine ZnInS) to 2.64 V (B25-**ZnInS**) versus the standard hydrogen electrode (versus SHE), while the conduction band minimum potential (E_{CB}) also undergoes a downward displacement from -0.71 to -0.47 V (versus SHE, calculated via $E_{\rm CB} = E_{\rm VB} - E_{\rm g}$). The complete band alignment diagram is presented in Figure 2a, illustrating that all of the as-prepared samples are thermodynamically favorable for O₂ photoreduction to H₂O₂ and H₂O oxidation to H_2O_2 . The systematic downward shift in the energy level of Bx-ZnInS photocatalysts directly correlates with electronwithdrawing effect of boron.[40] The downward shift of the $E_{\rm VB}$ position enhances the thermodynamic driving force for oxidation reactions, thereby beneficial to improve the overall photocatalytic redox efficiency.[41]

To unravel the electronic structure modulation induced by boron doping, density functional theory (DFT) calculations were performed to analyze the partial density of states (PDOS) and frontier orbital distributions. In pristine **ZnInS**

(Figure 2b), the VB maximum is primarily contributed by a filled S 3p and Zn 3d states, while the CB minimum is mainly composed of empty antibonding In 5s/5p state, indicating that the VB-to-CB transition is largely from filled S 3p/Zn 3d states to dominantly In 5s/5p state. Interestingly, upon the introduction of boron into ZnInS (Figure 2c), its electronic fine structure underwent partial adjustments, and the CB minimum is primarily contributed by the B 2p and In 5s/5porbitals. These results indicate that in **ZnInS**, photogenerated electrons and holes predominantly localize at the In site and Zn-S region, respectively, whereas boron doping in B-ZnInS shifts electron accumulation to In-B hybrid sites while maintaining hole confinement at Zn-S region. Therefore, a distinct spatial region distribution is observed between the highest occupied molecular orbital (HOMO) and the lowest unoccupied molecular orbital (LUMO), as clearly illustrated in Figure 2d,e. In the **B-ZnInS** system, the HOMO predominantly arises from Zn-S bonding configurations, while the LUMO primarily originates from synergistic In-B metalmetalloid interactions-a distinct electronic configuration that fundamentally differs from the isolated In sites dominating the LUMO characteristics in pristine **ZnInS**. From HOMO-LUMO phase distribution clearly indicates that the In-B sites in **B-ZnInS** serve as the potential reduction reaction sites, while the potential oxidation reaction sites of B-ZnInS are at the Zn-S sites.

The in situ light-irradiated-XPS (ISI-XPS) analysis revealed distinct shifts in binding energies of constituent elements upon light irradiation, providing direct evidence for catalytic sites distribution as well as photogenerated charge redistribution in B-ZnInS and ZnInS (Figures 2f, \$16, and \$17; data summarized in Table \$4). Specifically, the In 3d orbital exhibits a negative binding energy shift $(\Delta BE = -0.2 \text{ eV})$, while concurrent positive shifts were observed for both S 2p ($\Delta BE = +0.2 \text{ eV}$) and Zn 3d orbitals $(\Delta BE = +0.2 \text{ eV})$ (Figure S16). This complementary energy shift pattern strongly indicates the preferential accumulation of photogenerated electrons at In sites and hole localization at the Zn-S region, respectively. These experimental observations align well with the theoretical charge distribution prediction (Figure 2b,d). Notably, the binding energy values of In/B in B-ZnInS upon illumination both present negative shifts (Figure S17, $\triangle BE = -0.2 \text{ eV}$ for In and $\triangle BE = -0.3 \text{ eV}$ for B), suggesting the formation of the In-B dual-active centers. This is beneficial for the modulation of O₂ adsorption configurations from the single-site Pauling adsorption to the dual-site Yeager adsorption configuration (Figure 2g).

Adsorption, Activation, and Photogenerated Carrier Dynamics

The adsorption behavior and carrier dynamics, governed by electronic structure, were elucidated through combined experimental and theoretical approaches. Temperature-programmed desorption (TPD) directly assessed the O_2 adsorption capacity of the photocatalysts. **B-ZnInS** exhibits significantly enhanced O_2 adsorption compared to pristine **ZnInS**, with a three-fold increase in adsorption strength and a 20 °C rise in desorption temperature (Figure 3a), indicating



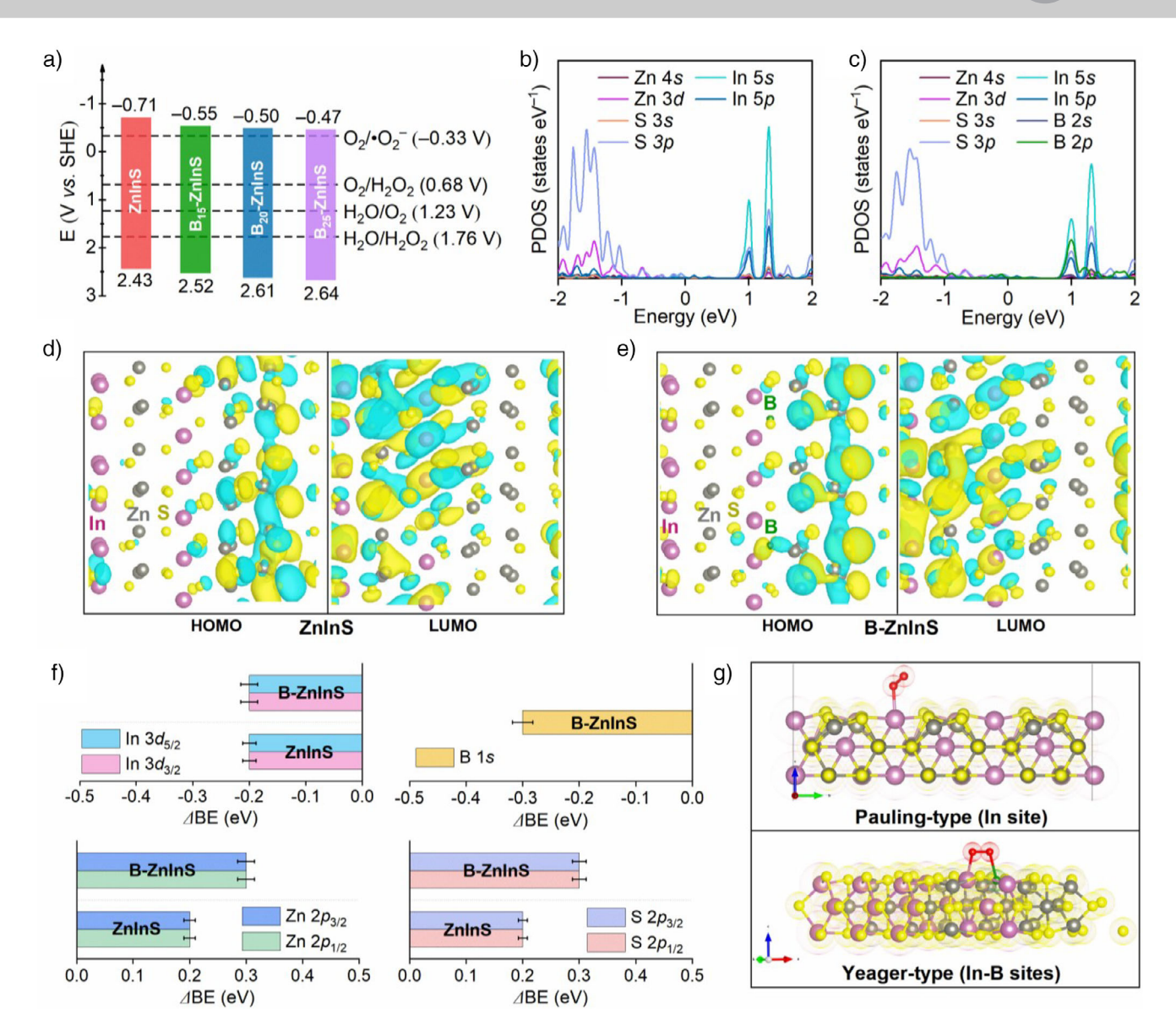


Figure 2. a) Schematic illustration of the **ZninS** and **B-ZninS** band structures. b), c) Partial density of states (PDOS) for **ZninS** and **B-ZninS**. Calculated HOMO and LUMO distributions of d) **ZninS** and e) **B-ZninS**. f) Light-induced shifts (Δ BE) in In 3d, B 1s, Zn 2p, and S 2p binding energy values from ISI-XPS for **ZninS** and **B-ZninS**. g) O₂ absorption configurations over **ZninS** and **B-ZninS**.

that boron atoms act as active centers for O2 activation. In addition, B-ZnInS exhibits a lower water contact angle and a higher zeta potential compared to pristine ZnInS (Figures \$18 and \$19), indicating that boron-induced local structural polarization strengthens dipole-dipole interactions with water.[42,43] The enhanced hydrophilicity and O2 affinity synergistically promote O₂ adsorption and protonation, thereby improving the 2e⁻ ORR efficiency for H₂O₂ production. Figures 3b and S20 show the optimized models and adsorption energy (E_{ads}) of the O_2 molecule adsorbed on the In site of pristine **ZnInS** as well as the In site, B site, and In-B dual sites of **B-ZnInS**, respectively. The E_{ads} of O_2 on the In-B dual sites in **B-ZnInS** is -0.51 eV, significantly lower than those on single In site (-0.28 eV) in **ZnInS** as well as single In site (-0.32 eV) and single B site (-0.18 eV) in **B-ZnInS**, indicating stronger O₂ adsorption at the boron-modified dual active sites. This suggests that **B-ZnInS** tends to adsorb O_2 at dual sites in a Yeager adsorption configuration, demonstrating a marked contrast to the adsorption behavior observed in **ZnInS**.

The charge density difference diagrams in Figure 3c reveal enhanced charge redistribution during O₂ adsorption. Compared with **ZnInS**, **B-ZnInS** exhibits more charge depletion and accumulation at the catalyst-O₂ interface, demonstrating superior O₂ activation capability through constructing dual carrier transfer channels. Moreover, the O–O bond length only slightly elongates from 1.21 (in gaseous O₂) to 1.24 Å, which is significantly below the critical breaking threshold (>1.33 Å) for the 4e⁻ pathway. This can be attributed to the In-B dual-sites charge complementation effect. Charge density difference maps reveal boron-induced charge redistribution in **B-ZnInS**. As shown in Figure 3d,

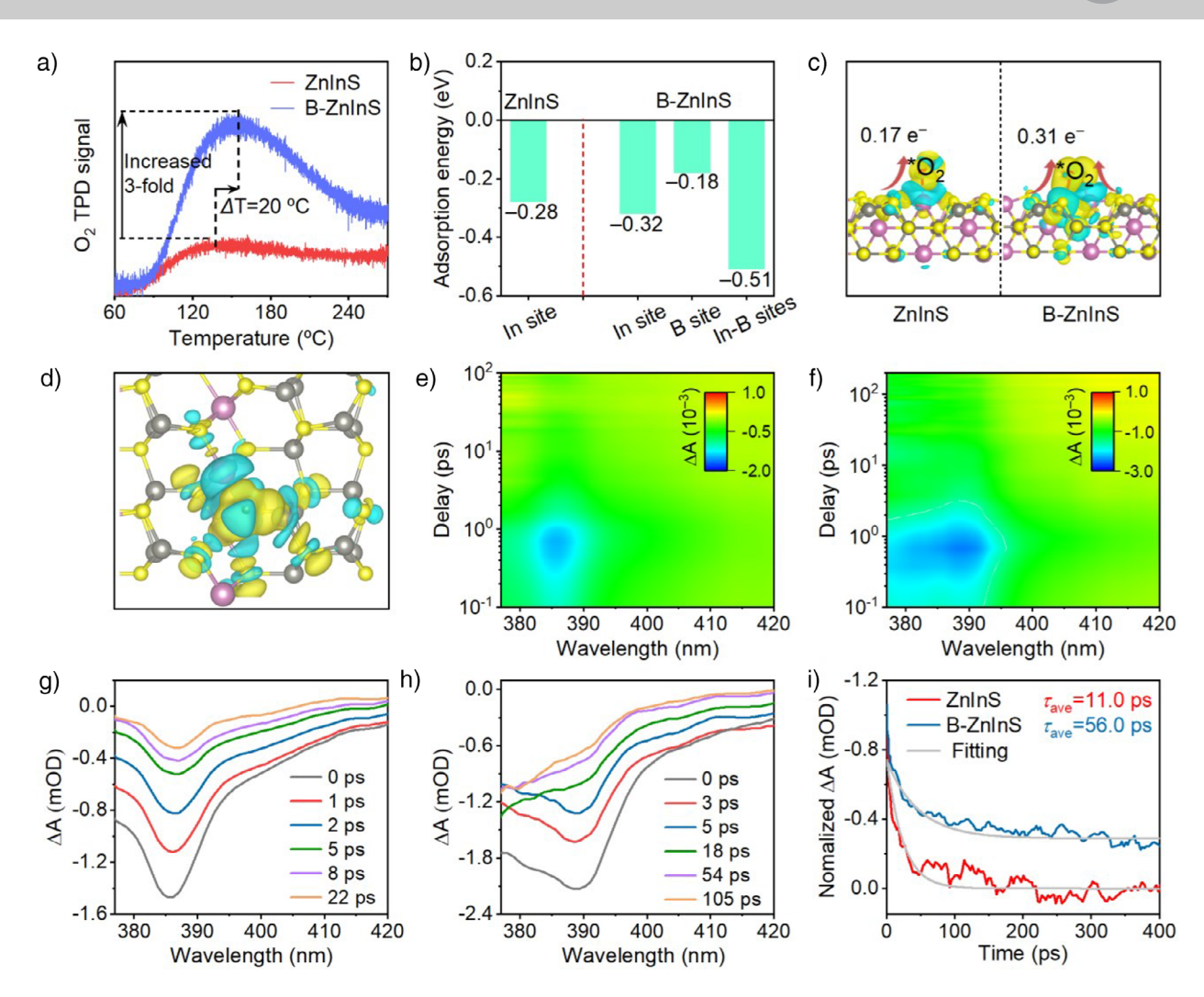


Figure 3. a) O₂-TPD spectra of **ZninS** and **B-ZninS**. b) O₂ adsorption energy of In site and In-B dual sites. c) Difference charge density stereograms of adsorbed O₂ on the In site of **ZninS** and In-B dual sites of **B-ZninS**, respectively. Yellow and cyan represent charge accumulation and depletion, respectively. d) Localized charge density distribution of **B-ZninS**. fs-TA spectra of e), g) **ZninS** and f), h) **B-ZninS**. i) TA dynamics probed at 386 nm.

B-ZnInS exhibits a distinct surface charge redistribution near the boron site region, and partial charge transfer occurs from the indium sites to the neighboring boron sites due to relative electron-deficient properties. The charge redistribution induced by the elemental complementarity effect results in the formation of a balanced electron reservoir in the In-B region, which modulates orbital coupling strength with O_2 , preventing excessive population of π^* antibonding orbitals that would destabilize the O–O bond. Furthermore, the localized polarized field stemming from structural polarization could facilitate spatially separating the photogenerated electron-hole pairs, thus suppressing recombination and improving charge transfer dynamics. [44]

The photogenerated carrier properties were analyzed by femtosecond transient absorption (fs-TA) spectroscopy and photoelectrochemical characterization. Figure 3e-h present the fs-TA spectra of **ZnInS** and **B-ZnInS** under 340 nm pump pulse excitation, revealing a pronounced negative peak spanning 375–420 nm, as recorded at selected probe delay times. This characteristic spectral feature is attributed to ground-state bleach (GSB), indicative of excited-state relax-

ation dynamics.^[45] Specifically, **B-ZnInS** exhibits a longer GSB recovery time than ZnInS, which is attributed to the prolonged excited-state lifetime resulting from improved charge separation induced by localized polarization. As depicted in Figure 3i and Table S5, the short lifetime component (τ_1) originates from the direct recombination of photogenerated carriers, while the long lifetime component (τ_2) is attributed to carriers retention after charge separation. Upon boron doping, τ_2 is prolonged from 28.1 to 82.0 ps with its relative contribution increasing from 29% to 67%, leading to an enhancement of the average carrier lifetime from 11.0 to 56.0 ps. This suggests that the localized polarization effectively suppresses charge recombination and improves charge separation. The steady and transient state photoluminescence (PL) spectra were measured to further investigate the photogenerated carrier dynamics. In pristine ZnInS, photogenerated electron-hole pairs predominantly undergo radiative recombination, manifested by intense PL emission (Figure S21a). In contrast, the built-in electric field in **B-ZnInS** accelerates charge separation, thereby suppressing electron-hole recombination and leading to a significant

15213773, 0, Downloaded from https://onlinelibrary.wiley.com/doi/10.1002/anie.202506963 by Tianjin University Of, Wiley Online Library on [24.062025]. See the Terms and Conditions (https://onlinelibrary.wiley.com/terms-and-conditions) on Wiley Online Library for rules of use; OA articles are governed by the applicable Creative Commons. Licenson

Research Article



reduction in PL intensity. As shown in Figure \$21b and Table S6, the transient PL decay of ZnInS is dominated by a fast decay component (lifetime $\tau_{AVE} = 0.7$ ns), which can be attributed to rapid charge recombination. Remarkably, B-ZnInS exhibits a prominent slow decay component (lifetime $\tau_{\rm AVE} = 3.8$ ns) owing to enhanced charge separation efficiency, corresponding to delayed recombination of spatially separated carriers. This prolonged lifetime implies a higher probability for the carriers in **B-ZnInS** to migrate effectively to the surface participating in molecular activation processes. [46] In addition, **B-ZnInS** demonstrates a significantly enhanced photocurrent response compared to pristine **ZnInS** (Figure \$22), facilitating greater charge accumulation for efficient reactant activation. Consistent with this, electrochemical impedance spectroscopy (EIS) measurements under illumination (Figure S23) revealed reduced charge transfer resistance in **B-ZnInS**, confirming improved photogenerated carrier transport and separation efficiency. Moreover, the non-equilibrium carrier concentrations can be calculated by the Mott–Schottky curves (Figure S24), and **B-ZnInS** possesses a reduced slope relative to ZnInS, indicating enhanced non-equilibrium carrier density. Quantitative calculations yielded carrier concentrations of $3.12 \times 10^{20} \text{ cm}^{-3}$ for **ZnInS**. In contrast, $12.70 \times 10^{20} \text{ cm}^{-3}$ for **B-ZnInS** (Table **S7**). This increased carrier population facilitates more efficient participation in redox processes, thereby enhancing photocatalytic performance.^[47]

Photocatalytic H₂O₂ Synthesis

H₂O₂ photosynthesis was performed in a custom-designed recirculation reactor (Figure 4a) with oxygen-saturated water as the reaction medium. H₂O₂ yields were quantified by iodometric titration (see, Figure \$25 for experimental details).^[48] As shown in Figure 4b, the H₂O₂ production of all catalysts gradually accumulates over time, indicating that the H₂O₂ photosynthesis reaction can be driven under the action of four catalysts prepared. Pristine **ZnInS** exhibits limited H₂O₂ production (440 µmol g⁻¹ after 120 min), whereas boron doping significantly enhances photocatalytic activity. The H₂O₂ production efficiency varies significantly with boron doping content, demonstrating tunable catalytic responsiveness to compositional modification. This observation provides preliminary evidence that boron incorporation plays a crucial role in enhancing H₂O₂ production by modulation of electronic structure and photogenerated carrier dynamics. Excessive boron doping can cause local structure overdistortion, resulting in carrier recombination, thus inhibiting catalytic performance (Figures S24, S26, and Table S7). As illustrated in Figure 4c, the B_{20} -ZnInS catalyst exhibits notable photocatalytic performance, achieving the highest H₂O₂ production rate of 3121 µmol g⁻¹ h⁻¹ in pure water under simulated sunlight irradiation, which represents an 11fold enhancement compared to pristine ZnInS. Remarkably, the system achieves an excellent apparent quantum yield (AQY) of 49.8% at 365 nm, outperforming the state-of-theart inorganic semiconductor photocatalysts reported to date (Figures 4d, S27, S28, and Table S8). Furthermore, it achieves 0.59% solar-to-chemical conversion efficiency, representing a 4.9-fold improvement over average natural photosynthesis (0.10%). Critically, scaled-up experiments confirm practical viability, with continuous production of medical-grade $\rm H_2O_2$ solution (3 wt%) under 48 h illumination (Figure S29 and Table S9).

To further elucidate the reaction process for H₂O₂ production, control experiments were conducted. As shown in Figure 4e, in the absence of both light irradiation and catalyst, negligible amounts of H₂O₂ were detected in the reaction system, suggesting that the H₂O₂ synthesis is exclusively driven by light under the action of photocatalyst. In addition, significant variations in H₂O₂ production were observed under different atmospheric conditions (Ar, Air, and O₂). The **B-ZnInS** catalyst exhibits optimal H₂O₂ generation in the O₂ atmosphere, while a dramatic decrease in production was detected under both Ar and air conditions. These results provide evidence that O₂ molecules serves as one of the primary sources for the H₂O₂ formation. Notably, **B-ZnInS** maintains a non-negligible H₂O₂ production even under the Ar atmosphere, implying that the water oxidation reaction (WOR) serves as an alternative pathway for H₂O₂ generation. As illustrated in Figure \$30, B-ZnInS displays an enhancement in H₂O₂ production in the presence of KBrO₃ (electron quencher), further suggesting that water oxidizes to H₂O₂ in the reaction system. This implies a dualpathway mechanism where H₂O₂ is co-generated through the 2e- ORR and the 2e- WOR. To definitively ascertain the origin of H₂O₂ synthesis, isotopic labeling experiments of ¹⁸O₂ and H₂¹⁸O were conducted by using mass spectra to detect O₂ evolved from MnO₂-catalyzed H₂O₂ decomposition (as described in Supporting Information).^[49] As depicted in Figure S31a, the detection of ${}^{18}O_2$ (m/z = 36) suggests the involvement of the ORR in the H₂O₂ synthesis process. When employing H₂¹⁸O as the H₂O source (Figure S31b), the detection of ${}^{18}\text{O}_2$ suggests the involvement of the WOR in the H₂O₂ synthesis process. Based on the above discussions, we can conclusively determine that the H₂O₂ photosynthesis in the reaction system is synergistically facilitated by both the 2e ORR and the 2e WOR processes.

The H_2O_2 production capability of the synthesized **B**-**ZnInS** samples was further evaluated through rotating ring-disk electrode (RRDE) measurements conducted in an oxygen-saturated 0.1 M Na₂SO₄ electrolyte under controlled electrochemical conditions.^[50] As illustrated in Figure 4f, the disk current (lower curve) reflects the total oxygen reduction reaction (ORR) activity, while the ring current (upper curve) specifically monitors the two-electron transfer pathway (2e⁻ ORR). All samples exhibit discernible ring and disk currents beyond-0.2 V (versus SHE), indicating the initiation of ORR processes and concomitant H₂O₂ generation. Notably, boron doping induces significant regulations in the current response profiles (Figure S32), with the B20-ZnInS composite demonstrating optimal performance that aligns with its superior photocatalytic H₂O₂ production activity. These current profile variations can be attributed to the optimized catalytic kinetics achieved through boron-mediated regulation of active sites. Complementary analysis of the average electron transfer number (n) calculated by Koutecky–Levich plots reveals that B_{20} -ZnInS exhibits an n-value approaching

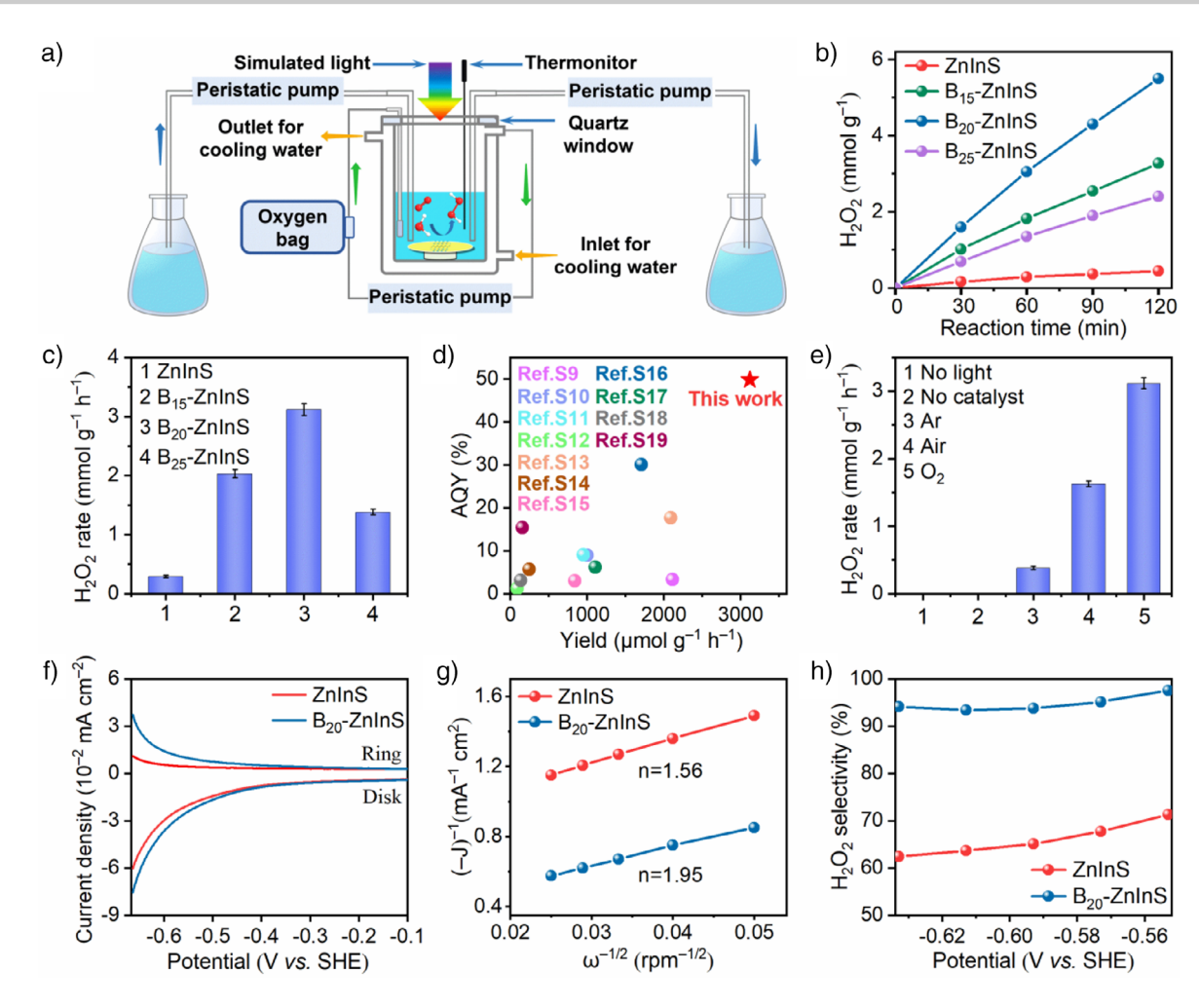


Figure 4. a) Schematic illustration of self-assembled photocatalytic recirculation reactor system. b) Time-dependent photocatalytic H_2O_2 production and c) the H_2O_2 generation rates. d) H_2O_2 photosynthesis performance of **B-ZnInS** with that of reported photocatalysts. e) H_2O_2 production under different atmospheres of **B-ZnInS**. f) RRDE polarization curves, g) the fitted K-L plots, and h) the corresponding H_2O_2 selectivity of **ZnInS** and **B-ZnInS**.

two compared to 1.5, 1.86, and 1.68 for pristine **ZnInS B**₁₅-ZnInS, and B₂₅-ZnInS, respectively (Figures 4g, S33, and \$34), demonstrating enhanced utilization of photogenerated charges for selective H₂O₂ synthesis. This corresponds to a remarkable improvement in H_2O_2 selectivity, with B_{20} -**ZnInS** achieving 95% selectivity versus 62%, 82%, and 74% for pristine ZnInS, B₁₅-ZnInS, and B₂₅-ZnInS, respectively (Figures 4h and S34c). The lower selectivity observed in **ZnInS** suggests competitive generation of highly oxidizing byproducts through alternative reaction pathways, potentially destabilizing the reaction system.^[51] The aforementioned performance variations unequivocally demonstrate the superiority of the In-B dual-site configuration in activating O₂ molecules. Furthermore, these findings suggest that ZnInS and **B-ZnInS** may follow divergent O₂ activation pathways: ZnInS likely favors an indirect two-step ORR mechanism for H₂O₂ generation, whereas **B-ZnInS** facilitates direct O₂-to-H₂O₂ conversion through optimized dual-site coordination. Post-reaction analyses of XRD patterns (Figure \$35), XPS spectra (Figure S36), and TEM images (Figures S37, S38, and Table \$10) reveal the structural components remaining intact in **B-ZnInS**, confirming its robust stability in the reaction system. In contrast, pristine **ZnInS** exhibits structural degradation (Figures S39–S42 and Table S11), showing a large change of structural components, likely caused by oxidative etching from reactive oxygen species generated through 1e⁻ ORR pathways.

Reaction Mechanisms for Photocatalytic H₂O₂ Synthesis

To probe the H_2O_2 photosynthesis mechanism, in situ diffuse reflectance infrared Fourier transform spectroscopy (DRIFTS) was employed to track real-time intermediates during O_2 activation. Figure 5a depicts the time-resolved in situ DRIFTS profiles of **ZnInS** and **B-ZnInS**. During the initial activation phase, both catalysts display characteristic vibrational signatures: **ZnInS** shows a distinct peak at 1200 cm⁻¹ while **B-ZnInS** exhibits a red-shifted band at 1100 cm⁻¹, corresponding to the chemisorbed *O_2 species with Pauling and Yeager adsorbed O_2 geometries, respectively. $^{[52,53]}$ This 100 cm^{-1} redshift stems from stronger

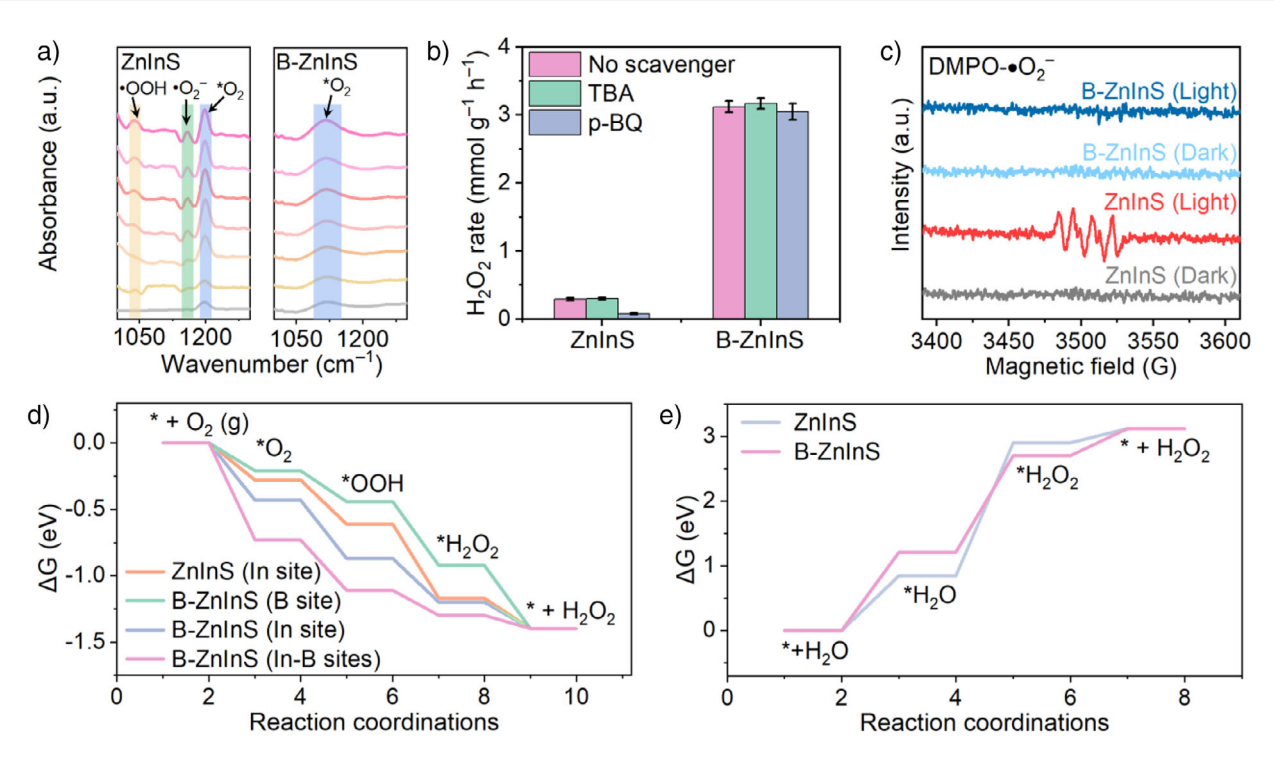


Figure 5. a) In situ DRIFTS spectra of (a) ZnInS and B-ZnInS. b) Comparison with H_2O_2 production under different reaction conditions. c) EPR spectra under light and dark conditions. Calculated free-energy diagrams of d) ORR and e) WOR pathways toward H_2O_2 production.

In-B dual-site interaction with O_2 , which lower the σ^* orbital energy of chemisorbed O_2 , [54] as supported by DFT calculations in Figure 3c. This facilitates electron injection into antibonding orbitals for oxygen reduction. With the progress of the reaction, the formation and enhancement of the O_2 species signal indicates that the O_2 activation process continues. Notably, the **ZnInS** sample exhibits distinct ${}^{\bullet}O_2{}^-$ and ${}^{\bullet}OOH$ absorption peaks at approximately 1150 cm⁻¹ and 1050 cm⁻¹, respectively, whereas these signals are absent in **B-ZnInS**. [55,56] This observation implies that **ZnInS** are more likely to follow the two-step $2e^-$ ORR pathway to produce H_2O_2 , while **B-ZnInS** follow a direct one-step two-electron ORR.

To further determine the roles of reactive species in H₂O₂ generation and reveal the reaction process, quenching experiments were performed using p-benzoquinone (p-BQ) and tert-butanol (TBA) as specific scavengers for •O₂⁻ and •OH, respectively (Figure 5b).[57] Of note, the production of H₂O₂ on **ZnInS** is significantly inhibited upon the addition of p-BQ, whereas the performance of B-ZnInS remains unaffected. Evidently, •O₂⁻ serves as a crucial intermediate for H₂O₂ synthesis over **ZnInS** catalyst, while the generation of H₂O₂ on **B-ZnInS** does not involve •O₂⁻, suggesting that the introduction of boron modulates the reaction pathway from a two-step 2e⁻ ORR process to a one-step 2e⁻ route. In addition, the production of H₂O₂ on both ZnInS and B-ZnInS remains unaffected upon the addition of TBA, indicating that the H₂O₂ synthesis at the oxidation side does not involve •OH and proceeds via a direct one-step 2e- WOR process. Moreover, EPR was conducted to detect •O2- and •OH with 5,5-dimethyl-1-pyrroline N-oxide (DMPO) as the spintrap agent. [58-60] Figure 5c reveals that **ZnInS** displays clear

DMPO- ${}^{\bullet}O_2^-$ characteristic signals under light, whereas **B-ZnInS** shows no DMPO- ${}^{\bullet}O_2^-$ signals under both light and dark conditions, suggesting that boron doping substantially inhibits the formation of ${}^{\bullet}O_2^-$. Based on the above results, it is rationally inferred the ORR for H_2O_2 generation mechanisms: **ZnInS** proceeds via a two-step $2e^-$ pathway involving ${}^{\bullet}O_2^-$ intermediates, boron-functionalized **B-ZnInS** facilitates direct one-step $2e^-$ ORR, bypassing reactive oxygen species and thereby improving H_2O_2 yield. Figure S43 shows that no ${}^{\bullet}OH$ signals were observed for all the samples, confirming H_2O is directly oxidized to H_2O_2 by the one-step $2e^-$ WOR process at the oxidation side.

The Gibbs free energies of ORR and WOR over ZnInS and **B-ZnInS** were further calculated to reveal the intermediate evolution in the photocatalytic H₂O₂ synthesis. According to the different active center locations of different catalysts, we constructed four configurations, named ZnInS (In site), B-ZnInS (B site), B-ZnInS (In site), and B-ZnInS (In-B sites). As shown in Figure 5d, the downward-trending Gibbs free energy of all photocatalysts in the 2e⁻ pathway indicates the thermodynamic feasibility of H₂O₂ generation on **ZnInS** and **B-ZnInS.** For the O₂ adsorption initiation step, the In-B dualactive center sites on **B-ZnInS** demonstrate a significantly reduced Gibbs free energy change ($\Delta G = -0.41 \text{ eV}$) compared to other adsorption sites, which is attributed to the synergistic effect of the In-B dual-sites configuration that facilitates enhanced O2 adsorption and activation. Moreover, compared with the other adsorption configurations, B-**ZnInS** (In-B sites) displays the lowest ΔG for •OOH and •HOOH intermediates, suggesting the constructed In-B dual active sites accelerates the proton-coupled electron transfer process promoting the H₂O₂ synthesis. Thereby, this reduces

15213773, 0, Downloaded from https://onlinelibrary.wiley.com/doi/10.1002/anie.202506963 by Tianjin University Of, Wiley Online Library on [24.062025]. See the Terms and Conditions (https://onlinelibrary.wiley.com/terms-and-conditions) on Wiley Online Library for rules of use; OA articles are governed by the applicable Ceataive Commons Licenses

the formation of •O₂⁻ intermediates and improves carrier utilization efficiency and reaction kinetics for efficient H₂O₂ synthesis. The E_{VB} of **ZnInS** and **B-ZnInS** (2.43 - 2.64 V versus SHE) lies above the direct 2e- WOR potential (1.76 V) but below the indirect pathway (2.73 V), favoring direct H₂O oxidation (Figure 2a). In the 2e⁻ WOR process (Figure 5e), compared with ZnInS, B-ZnInS possess lower energy barriers in the rate-determining step, which not only improves the 2e⁻ WOR reaction dynamics but also promotes the proton supply of $2e^-$ ORR reaction. The minimized ΔG for **B-ZnInS** protonation steps confirms that the introduction of boron accelerates the 2e- ORR/WOR kinetics through the modulation of electronic structure and photocarrier dynamics.

Conclusion

To summarize, we have developed a boron-modified zinc indium sulfide (B-ZnInS) photocatalyst that unlocks a direct one-step two-electron oxygen reduction pathway for efficient solar-driven H₂O₂ synthesis. According to theoretical calculation and ultrafast spectra dynamic characterization, the incorporation of boron induces In-B dual-sites, which synergistically regulate the electronic structure and photocarrier dynamics in B-ZnInS. This architecture balances O₂ activation strength to avoid O-O bond cleavage while enabling synchronous dual-channel electron injection into π^* orbitals. Concurrently, boron doping generates a polarized electric field, spatially segregating photogenerated carriers and extending their lifetime by five-fold. The intermediate quenching experiments and in situ FTIR spectroscopy demonstrate that these concerted effects shift the O2 reduction pathway from the two-step mechanism to a direct single-step 2e⁻ process. This system achieves a notable H₂O₂ production rate of 3121 µmol g⁻¹ h⁻¹ in pure water under simulated sunlight—11 times higher than pristine ZnInS. Remarkably, the system attains a record apparent quantum yield of 49.8% at 365 nm among inorganic photocatalysts, alongside a solar-to-chemical efficiency of 0.59%, surpassing natural photosynthesis. This work not only provides a rational design strategy for highly efficient H₂O₂ photocatalysts but also offers fundamental insights into modulating reaction pathways for diverse catalytic applications.

Acknowledgements

This work was financially supported by the National Key R&D Program of China (2022YFA1502902), NSFC (U21A20286, 22475152, and 22305214), Natural Science Foundation of Tianjin City (24JCYBJC00840), the 111 Project of China (D17003), and the Jiangsu Funding Program for Excellent Postdoctoral Talent (2022ZB616).

Conflict of Interests

The authors declare no conflict of interest.

Data Availability Statement

The data that support the findings of this study are available from the corresponding author upon reasonable request.

Keywords: Charge separation • Dual-active sites • O₂ activation pathways • Photocatalytic H₂O₂ synthesis

- [1] Y. Zhang, C. Pan, G. Bian, J. Xu, Y. Dong, Y. Zhang, Y. Lou, W. Liu, Y. Zhu, Nat. Energy 2023, 8, 361-371.
- J. K. Edwards, B. Solsona, E. N. N., A. F. Carley, A. A. Herzing, C. J. Kiely, G. J. Hutchings, Science 2009, 323, 1037–1041.
- [3] Y. Liu, L. Li, Z. Sang, H. Tan, N. Ye, C. Sun, Z. Sun, M. Luo, S. Guo, Nat. Synth. 2025, 4, 134-141.
- [4] K. Li, Q. Ge, Y. Liu, L. Wang, K. Gong, J. Liu, L. Xie, W. Wang, X. Ruan, L. Zhang, Energy Environ. Sci. 2023, 16, 1135-1145.
- [5] W. Chi, Y. Dong, B. Liu, C. Pan, J. Zhang, H. Zhao, Y. Zhu, Z. Liu, Nat. Commun. 2024, 15, 5316.
- [6] H. Li, Y. Li, X. Lv, C. Liu, N. Zhang, J. Zang, P. Yue, Y. Gao, C. Liu, Y. Li, Adv. Mater. 2025, 37, 2415126
- [7] J. Y. Choi, B. Check, X. Fang, S. Blum, H. T. B. Pham, K. Tayman, J. Park, J. Am. Chem. Soc. 2024, 146, 11319–11327.
- [8] J.-Y. Yue, L.-P. Song, Y.-F. Fan, Z.-X. Pan, P. Yang, Y. Ma, Q. Xu, B. Tang, Angew. Chem. Int. Ed. 2023, 62, e202309624.
- [9] Y. Sun, Z. Qian, M. Sun, Y. Li, Q. Zhang, Y. Nie, L. Gu, M. Luo, J. Liu, B. Huang, S. Guo, Chem. 2025, 11, 102393.
- [10] W. Li, B. Han, Y. Liu, J. Xu, H. He, G. Wang, J. Li, Y. Zhai, X. Zhu, Y. Zhu, Angew. Chem. Int. Ed. 2025, 64, e202421356.
- [11] Z. Zhuang, A. Huang, X. Tan, K. Sun, C. Chen, Q. Peng, Z. Zhuang, T. Han, H. Xiao, Y. Zeng, W. Yan, J. Zhang, Y. Li, Joule **2023**, 7, 1003–1015.
- [12] W. Wu, Z. Li, S. Liu, D. Zhang, B. Cai, Y. Liang, M. Wu, Y. Liao, X. Zhao, Angew. Chem. Int. Ed. 2024, 63, e202404563.
- [13] L. Liu, M.-Y. Gao, H. Yang, X. Wang, X. Li, A. I. Cooper, *J. Am.* Chem. Soc. 2021, 143, 19287-19293.
- [14] M. Sun, X. Wang, Y. Li, H. Pan, M. Murugananthan, Y. Han, J. Wu, M. Zhang, Y. Zhang, Z. Kang, ACS Catal. 2022, 12, 2138-
- [15] D. Jiao, C. Ding, M. Xu, X. Ruan, S. K. Ravi, X. Cui, Adv. Funct. Mater. 2025, 35, 2416753.
- [16] P. Liu, T. Liang, Y. Li, Z. Zhang, Z. Li, J. Bian, L. Jing, Nat. Commun. 2024, 15, 9224.
- [17] C. Chen, M. Wu, Y. Xu, C. Ma, M. Song, G. Jiang, J. Am. Chem. Soc. 2024, 146, 9163-9171.
- [18] C. Feng, J. Alharbi, M. Hu, S. Zuo, J. Luo, H. S. A.l Qahtani, M. Rueping, K.-W. Huang, H. Zhang, Adv. Mater. 2025, 37, 2406748.
- [19] L. Xie, P. Wang, Y. Li, D. Zhang, D. Shang, W. Zheng, Y. Xia, S. Zhan, W. Hu, Nat. Commun. 2022, 13, 5560.
- [20] X. Zhang, D. Gao, B. Zhu, B. Cheng, J. Yu, H. Yu, Nat. Commun. 2024, 15, 3212.
- [21] C. Zhu, Y. Yao, Q. Fang, S. Song, B. Chen, Y. Shen, ACS Catal. **2024**, 14, 2847–2858.
- [22] C. He, C.-H. Lee, L. Meng, H.-Y. T. Chen, Z. Li, J. Am. Chem. Soc. 2024, 146, 12395-12400.
- [23] Z. Wang, S. Liu, Y. Liu, X. Wei, N. Liang, Z. Sang, J. Jiang, B. Li, Small 2025, 21, 2410612.
- [24] S. Xu, X. Mi, P. Wang, Y. Mao, Q. Zhou, S. Zhan, Adv. Funct. Mater. 2023, 33, 2308204.
- [25] Z. Zhao, P. Wang, C. Song, T. Zhang, S. Zhan, Y. Li, Angew. Chem. Int. Ed. 2023, 62, e202216403.
- [26] M. Xiao, Y. Chen, J. Zhu, H. Zhang, X. Zhao, L. Gao, X. Wang, J. Zhao, J. Ge, Z. Jiang, S. Chen, C. Liu, W. Xing, J. Am. Chem. Soc. 2019, 141, 17763-17770.



15213773, 0, Downloaded from https://onlinelibrary.wiley.com/doi/10.1002/anie.202506963 by Tianjin University Of, Wiley Online Library on [24.062025]. See the Terms and Conditions (https://onlinelibrary.wiley.com/terms

on Wiley Online Library for rules of use; OA articles

are governed by the applicable Creative Commons

- [27] Y. Bai, Y. Wu, X. Zhou, Y. Ye, K. Nie, J. Wang, M. Xie, Z. Zhang, Z. Liu, T. Cheng, C. Gao, *Nat. Commun.* 2022, *13*, 6094.
- [28] W. Liu, J. Chen, Y. Wei, Y. He, Y. Huang, M. Wei, Y. Yu, N. Yang, W. Zhang, L. Zhang, F. Saleem, F. Huo, Adv. Funct. Mater. 2024, 34, 2408732.
- [29] H. Peng, H. Yang, J. Han, X. Liu, D. Su, T. Yang, S. Liu, C.-W. Pao, Z. Hu, Q. Zhang, Y. Xu, H. Geng, X. Huang, J. Am. Chem. Soc. 2023, 145, 27757–27766.
- [30] E. Pastor, M. Sachs, S. Selim, J. R. Durrant, A. A. Bakulin, A. Walsh, *Nat. Rev. Mater.* 2022, 7, 503–521.
- [31] J. Wang, T. Xia, L. Wang, X. Zheng, Z. Qi, C. Gao, J. Zhu, Z. Li, H. Xu, Y. Xiong, Adv. Mater. 2018, 57, 16447–16451.
- [32] J. Luo, X. Wei, Y. Qiao, C. Wu, L. Li, L. Chen, J. Shi, Adv. Mater. 2023, 35, 2210110.
- [33] T. Yuan, L. Sun, Z. Wu, R. Wang, X. Cai, W. Lin, M. Zheng, X. Wang, Nat. Catal. 2022, 5, 1157–1168.
- [34] L.-P. Chi, Z.-Z. Niu, X.-L. Zhang, P.-P. Yang, J. Liao, F.-Y. Gao, Z.-Z. Wu, K.-B. Tang, M.-R. Gao, Nat. Commun. 2021, 12, 5835.
- [35] D.-Y. Wei, M.-F. Yue, S.-N. Qin, S. Zhang, Y.-F. Wu, G.-Y. Xu, H. Zhang, Z.-Q. Tian, J.-F. Li, J. Am. Chem. Soc. 2021, 143, 15635–15643.
- [36] X. Wang, X. Wang, J. Huang, S. Li, A. Meng, Z. Li, Nat. Commun. 2021, 12, 4112.
- [37] M. Wang, G. Zhao, X. Bai, W. Yu, C. Zhao, Z. Gao, P. Lyu, Z. Chen, N. Zhang, Adv. Energy Mater. 2023, 13, 2301730.
- [38] Y. Pan, X. Liu, W. Zhang, B. Shao, Z. Liu, Q. Liang, T. Wu, Q. He, J. Huang, Z. Peng, Y. Liu, C. Zhao, *Chem. Eng. J.* 2022, 427, 132032
- [39] T. Xu, Z. Wang, W. Zhang, S. An, L. Wei, S. Guo, Y. Huang, S. Jiang, M. Zhu, Y.-B. Zhang, W.-H. Zhu, J. Am. Chem. Soc. 2024, 146, 20107–20115.
- [40] D. Zhao, Y. Wang, C.-L. Dong, Y.-C. Huang, J. Chen, F. Xue, S. Shen, L. Guo, *Nat. Energy* 2021, 6, 388–397.
- [41] K. Zhang, L. Tian, J. Yang, F. Wu, L. Wang, H. Tang, Z.-Q. Liu, Angew. Chem. Int. Ed. 2024, 63, e202317816.
- [42] M. Rafiq, K. Harrath, M. Feng, R. Li, A. R. Woldu, P. K. Chu, L. Hu, F. Lu, X. Yao, Adv. Energy Mater. 2024, 14, 2402866.
- [43] P. Han, X. Yang, L. Wu, H. Jia, J. Chen, W. Shi, G. Cheng, W. Luo, Adv. Mater. 2024, 36, 2304496.
- [44] S. Meng, J. Li, S. Wang, S. Zhan, W. Hu, Y. Li, Adv. Mater. 2025, 37, 2420080.
- [45] Y.-F. Mu, H.-L. Liu, M.-R. Zhang, H.-J. Wang, M. Zhang, T.-B. Lu, J. Energy Chem. 2023, 77, 317–325.

- [46] Y.-F. Mu, J.-S. Zhao, L.-Y. Wu, K.-Y. Tao, Z.-L. Liu, F.-Q. Bai, D.-C. Zhong, M. Zhang, T.-B. Lu, Appl. Catal. B Environ. 2023, 338, 123024.
- [47] J.-S. Zhao, Y.-F. Mu, L.-Y. Wu, Z.-M. Luo, L. Velasco, M. Sauvan, D. Moonshiram, J.-W. Wang, M. Zhang, T.-B. Lu, Angew. Chem. Int. Ed. 2024, 63, e202401344.
- [48] X. Zhang, H. Su, P. Cui, Y. Cao, Z. Teng, Q. Zhang, Y. Wang, Y. Feng, R. Feng, J. Hou, X. Z. Gan, Y. Zhao, Q. Liu, T. Zhang, K. Zheng, Nat. Commun. 2023, 14, 7115.
- [49] H. Yu, F. Zhang, Q. Chen, P.-K. Zhou, W. Xing, S. Wang, G. Zhang, Y. Jiang, X. Chen, Angew. Chem. Int. Ed. 2024, 63, e202402297.
- [50] L. Li, J. Zhu, F. Kong, Y. Wang, C. Kang, M. Xu, C. Du, G. Yin, Matter 2024, 7, 1517–1532.
- [51] Y. Deng, W. Liu, R. Xu, R. Gao, N. Huang, Y. Zheng, Y. Huang, H. Li, X. Kong, L. Ye, Angew. Chem. Int. Ed. 2024, 63, e202319216.
- [52] F. N. Hao, C. Yang, X. M. Lv, F. S. Chen, S. Y. Wang, G. F. Zheng, Q. Han, Angew. Chem. Int. Ed. 2023, 62, e202315456.
- [53] Y. Luo, B. Zhang, C. Liu, D. Xia, X. Ou, Y. Cai, Y. Zhou, J. Jiang, B. Han, Angew. Chem. Int. Ed. 2023, 62, e202305355.
- [54] X. Sun, J. Yang, X. Zeng, L. Guo, C. Bie, Z. Wang, K. Sun, A. K. Sahu, M. Tebyetekerwa, T. E. Rufford, X. Zhang, *Angew. Chem. Int. Ed.* 2024, 63, e202414417.
- [55] H. Zhang, W. X. Wei, K. Chi, Y. Zheng, X. Y. Kong, L. Q. Ye, Y. Zhao, K. A. I. Zhang, ACS Catal. 2024, 14, 17654– 17663.
- [56] R. Li, L. Zhang, X. Qin, S. Xu, C. Che, W. Wang, C. Zhang, W. Wang, ACS Catal. 2025, 15, 2171–2179.
- [57] G. Ba, H. Hu, F. Bi, J. Yu, E. Liu, J. Ye, D. Wang, Appl. Catal. B Environ. 2025, 361, 124645.
- [58] Z.-L. Liu, H.-Y. Luo, M.-R. Zhang, Y.-F. Mu, F.-Q. Bai, Chem. Eng. J. 2024, 491, 151913.
- [59] K. Zhang, M. Dan, J. Yang, F. Wu, L. Wang, H. Tang, Z.-Q. Liu, Adv. Funct. Mater. 2023, 33, 2302964.
- [60] K.-L. Zhang, H.-C. Chen, L. Wang, H. Tang, Z.-Q. Liu, Sci. Bull. 2025, 70, 536–545.

Manuscript received: March 27, 2025 Revised manuscript received: April 27, 2025 Accepted manuscript online: May 02, 2025

Version of record online:
,

Research Article

H₂O₂ Photosynthesis

Unlocking One-Step Two-Electron Oxygen Reduction via Metalloid Boron-Modified $Zn_3In_2S_6$ for Efficient H_2O_2 Photosynthesis

A boron-modified $Zn_3In_2S_6$ photocatalyst is engineered, featuring In-B dual-active sites that establish dual-channel carrier transfer pathways and substantially prolong photogenerated carrier lifetimes five-fold. These synergistic effects enable direct one-step $2e^-$ ORR for efficient H_2O_2 production from O_2 in pure water, achieving a record apparent quantum yield of 49.8% at 365 nm among inorganic semiconductor photocatalysts.

